



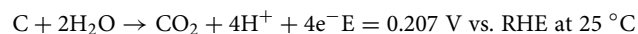
OPEN

Enhanced performance of proton exchange membrane fuel cells by Pt/carbon/antimony-doped tin dioxide triple-junction catalyst

Du-Cheng Tsai, Bing-Hau Kuo, Hung-Pin Chen, Erh-Chiang Chen & Fuh-Sheng Shieu✉

A composite material comprising carbon black and Sb-doped SnO₂ (ATO) is employed as a support for a Pt catalyst in a membrane electrode assembly (MEA) to improve the performance of a proton-exchange membrane fuel cell under low-humidity conditions. The effects of Sb-doping on the crystal, structural, and electrochemical characteristics of ATO particles are being examined. In a single cell test, the ratio of Sb in ATO is systematically optimized to improve performance. The distribution of Pt nanoparticles is uniform on carbon black and ATO carrier, forming notable triple-junction points at the interface of carbon black and ATO carrier. This structure thus induces a strong interaction between Pt and ATO, promoting the content of metallic Pt. Compared with a Pt/C catalyst, the best-performing Pt/C–ATO catalyst exhibits superior electrochemical activity, stability, and CO tolerance. The power density of MEA with the Pt/C–ATO catalyst is 15% higher than that of the MEA with the Pt/C catalyst

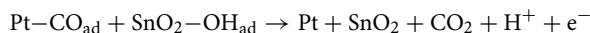
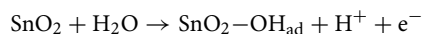
Proton exchange membrane fuel cells (PEMFCs) have emerged as highly promising energy sources due to their exceptional fuel utilization efficiency, low operational temperature, and environmental friendliness^{1–3}. Nevertheless, the commercialization of PEMFCs in industrial machinery and electric vehicles continues to face significant challenges regarding cost and reliability⁴. Pt catalysts supported on carbon black (Pt/C) are widely used as primary catalyst layers in PEMFCs. However, the catalytic activity of the Pt/C layer is vulnerable to degradation resulting from CO poisoning and carbon corrosion. In a conventional method of hydrogen production, hydrocarbon reforming is commonly employed because of its cost-effectiveness and high production rate. However, even after undergoing reforming, the resulting fuel may contain residual quantities of CO or comparable CO-like species at the parts-per-million (ppm) level⁵. Notably, CO at the ppm level has marked tendency to be adsorbed onto a Pt surface through a concerted electron transfer mechanism involving the transfer of electrons from the Pt d orbital to the C–O 2π* orbital and simultaneously from the CO 5σ orbital to the Pt orbital⁶. Previous research has demonstrated that even a mere concentration of 10 ppm of CO in a fuel gas can significantly diminish the catalytic activity of Pt catalysts in hydrogen oxidation and reduction reactions^{7–9}. Pt catalysts accelerate the corrosion of carbon support materials in PEMFCs¹⁰. Carbon black, known for its large surface area, high electrical conductivity, and low cost, is commonly utilized to disperse Pt nanocatalysts in PEMFCs. However, when employed as an electrode in PEMFCs, carbon black is exposed to corrosive conditions, such as high humidity, low pH, high potential (0.6–1.2 V), and elevated temperature (~80 °C). Under acidic and oxidative environments, carbon corrosion occurs as a thermodynamically plausible process, leading to the loss of carbon supports through their involvement in oxidation reactions during electrochemical processes, as depicted below^{11,12}:



Borup et al.¹³ demonstrated that carbon corrosion and Pt particle size within a catalyst layer increase with rising potential and decreasing humidity. Wang et al.¹⁴ investigated performance degradation attributed to Pt loss from a corroded carbon surface and enlargement of Pt particle size within a cathode catalyst layer. To address challenges posed by CO poisoning and carbon corrosion, considerable attention has been directed toward metal oxides. These materials offer high corrosion resistance, exhibit strong interactions with Pt catalysts that enhance activity, and can adsorb abundant hydroxyl groups, facilitating the removal of adsorbed CO-like intermediate species^{15–17}.

Department of Materials Science and Engineering, National Chung Hsing University, Taichung 40227, Taiwan, ROC.
✉email: fsshieu@nchu.edu.tw

TiO₂^{18,19}, Nb₂O₅²⁰, and SnO₂²¹ metal oxides are widely investigated as catalyst supports owing to their relatively high electrical conductivity, specific surface areas, and chemical stability. Among these metal oxides, SnO₂ stands out as an n-type semiconductor possessing superior electronic conductivity and cost-effectiveness. Pt–Sn-based catalysts incorporated with Sn demonstrates remarkable catalytic performance attributed to the ability of Sn to decrease Pt binding energy toward the negative side²². In addition, SnO₂ exhibits a co-catalytic effect through surface hydroxyls, as shown in the following formula^{23,24}.



The aforementioned reaction suggests that the incorporation of SnO₂ into a Pt catalyst facilitates CO oxidation, consequently improving the CO tolerance of Pt. However, the relatively low electrical conductivity and surface area of metal oxides compared with carbon hinders efficient electron transfer during electrochemical reactions. To address this limitation, combining metal oxides and carbon composite materials emerges as a promising approach for modifying electrical conductivity^{25–29}. González et al.³⁰ synthesized a composite catalyst consisting of Pt–SnO₂/C using a microwave-assisted polyol method. This composite catalyst demonstrated improved catalytic activity and stability for in methanol oxidation reaction, outperforming commercial Pt–Ru/C catalysts. Another method for improving the conductivity of SnO₂ is increasing the concentration of free electrons in the SnO₂ lattice by doping it with metal ions that possess a higher valence state than the native cations in SnO₂. This type of doping is known as cation doping. Lee et al.³¹ prepared the Pt/Sb-doped SnO₂ (ATO) catalyst via the polyol method. This catalyst exhibits significantly enhanced oxygen reduction reaction (ORR) activity and CO tolerance compared with Pt/C catalysts.

Current investigations have yet to yield a consensus on the precise Sb content that would constitute the most effective formulation for Pt–SnO₂/C electrocatalysts. This lack of consensus arises from the fact that the catalytic performance is profoundly reliant on an array of physicochemical traits of the synthesized Pt nanoparticles. To minimize the impact of ATO synthesis on Pt production, this study commenced with the synthesis of ATO/C nanocomposites, followed by the deposition of Pt nanoparticles onto the surface of the ATO/C. Different levels of Sb loading were incorporated to enhance the electrical conductivity of ATO and explore the optimal Sb doping concentration. Our homemade Pt/C results were employed as a reference for comparison with the findings discussed in this paper. We aimed to investigate the impact of Sb doping on the electrical conductivity of SnO₂ and the dispersion of Pt supported on ATO and carbon composite materials. On the other hand, the activity and performance of many related catalytic materials are evaluated by inducing the ORR in a sulfuric acid solution. Although ORR testing can screen and optimize catalysts at a preliminary stage, it cannot completely replace actual fuel cell tests. The testing in a fuel cell setup is crucial to fully evaluate the potential of a catalyst for practical applications. Therefore, we conducted an evaluation of their performance and stability in single-cell applications. The findings can enhance understanding of the conductivity and electrocatalytic properties of ATO nanoparticles and provide a foundation for the development of high-performance SnO₂-based materials for fuel cells.

Experimental

Catalyst preparation

The ATO/carbon black (C–ATO) particles were synthesized as follows: first, mixtures containing 1 g of carbon black (Vulcan XC-72, Cabot); 0.5 g of SnCl₂·2H₂O (ALFA); and 0.025, 0.05, or 0.1 g of SbCl₃ (ALFA) dissolved in hydrochloric acid were prepared. The mixtures were then labeled as C–ATO 5%, C–ATO 10%, and C–ATO 20%. These labels are based on the weight of Sb relative to the weight of Sn. The resulting mixtures were thoroughly dispersed by stirring in de-ionized water at 65 °C for 2 h and then treated with ammonia water for the precipitation of hydroxides onto the carbon black support until the pH reached 8.5. The resulting materials were subsequently filtered and dried in a vacuum oven at 105 °C for 12 h to produce C–ATO particles. The method used to prepare ATO particles was the same as that described earlier, but carbon black was not incorporated in the process. The Pt/C–ATO nanoparticles were synthesized using the impregnation method. Approximately 1 g of C–ATO nanoparticle was first added to deionized water and ultrasonicated for 2 h to obtain a good dispersion. Next, 0.66 g of H₂PtCl₆·6H₂O (Alfa Aesar), 10 mL of 1 M NaOH, and 10 mL of ethylene glycol (ALFA) were added to the solution, which was then refluxed in a three-necked flask at 85 °C for 4.5 h. Finally, the as-prepared Pt/C–ATO catalyst was filtered and dried in a vacuum oven at 85 °C for 12 h. A catalyst ink was prepared from the catalyst, Nafion solution (Dupont), and alcohol (Aldrich), which were mixed using an ultrasonicator for 2 h. The catalyst ink was then sprayed onto commercial carbon cloth (SGL-10BA, SIGRACET). The Pt/C–ATO catalysts were used on the cathode and anode. The Nafion 112 membrane was sandwiched between the anode and cathode and then hot-pressed under 85 kgf cm^{–2} for 2 min at 105 °C. Pt loading at the anode and cathode was 0.4 mg cm^{–2}, and the effective area of membrane electrode assembly (MEA) was 5 cm².

Characterization

The crystal structures were examined using an X-ray diffractometer (XRD, MacScience MXP3) equipped with Cu Kα radiation. The average grain size was determined using Scherrer's formula based on the full width at half-maximum. The morphology analysis was conducted using field emission scanning electron microscopy (SEM, JEOL JSM-6700F). Microstructural characterizations were conducted utilizing an analytical transmission electron microscope (TEM, JEM-2100F). The surface composition and chemical binding energies were investigated employing X-ray photoelectron spectroscopy (XPS, PHI 500 VersaProbe, ULVAC-PHI) equipped with monochromatic Al Kα radiation. The electrical conductivities were determined using the Van der Pauw

configuration. The cyclic voltammetry was performed using an electrochemical workstation (CHI 614B) to evaluate the electrochemically active surface area (ECSA) and methanol oxidation reaction (MOR) of the catalysts. The ECSA measurement utilized a 0.5 M H₂SO₄ electrolyte with a scan rate of 10 mV/s and a scan range of -0.4 to 1.2 V, while the MOR test employed a 0.5 M H₂SO₄ + 1 M CH₃OH electrolyte with the same scan rate and a scan range of 0 to 1.4 V. Ag/AgCl electrode served as the reference electrode, while Pt wires were employed as the counter electrode. The polarization curves of a single cell with a serpentine flow pattern were measured at a potential sweeping rate of 0.5 V min⁻¹ at room temperature using a fuel-cell test station (Beam 100 from Beam Associate Co., Ltd.). Hydrogen and oxygen were supplied to both the anode and cathode at a flow rate of 100 SCCM.

Results and discussion

Figure 1 illustrates the wide-angle diffraction patterns of Pt/C and Pt/C-ATO catalysts. The diffraction peaks corresponding to the crystalline planes of Pt at (111), (200), and (220) were observed at 2θ values of 39.85, 46.21, and 67.75, respectively, as compared with the JCPDS data file (No. 04-0802). Similarly, the diffraction peaks at 2θ values of 26.61, 33.89, 37.95, 38.97, and 51.78 can be assigned to the (110), (101), (200), and (211) planes of SnO₂ according to the JCPDS data file (No. 00-0411445). The absence of distinct diffraction peaks attributed to antimony oxide in the XRD pattern indicates the incorporation of Sb ions into the SnO₂ lattice or that antimony oxide is amorphous³¹. To estimate the crystalline sizes of Pt and ATO, Scherrer's equation³² was employed, and the results are presented in Table 1. The following phenomena were observed: (1) increase in Sb doping resulted in a notable decrease in the grain size of the SnO₂ phase (from 4.77 to 3.45 nm) probably because of the incorporation of Sb atoms, which introduce lattice defects and induce internal stress in the crystal lattice³³. Moreover, the presence of amorphous antimony oxide may have hindered the growth of SnO₂ crystals. (2) The addition of metal oxides had a certain impact on the size of the Pt particles. However, existing literature does not provide a clear answer regarding how the addition of metal oxides affects the sizes of Pt particles. In some cases, metal oxides can act as stabilizers or promoters for Pt nanoparticles. Metal oxide can interact with Pt nanoparticles through chemical bonding or electrostatic interactions, preventing agglomeration or coalescence and maintaining small particle sizes^{27,34-36}. However, metal oxides have lower surface areas than carbon black. This feature may promote particle aggregation and Pt growth, increasing particle size^{37,38}. Additionally, when an excess of metal oxides is added, the oxides tend to self-organize into larger clusters, which can lead to the clustering of Pt particles within the interstices of oxide aggregates, consequently decreasing the available surface area for the Pt particles. In the present study, the grain size of Pt is significantly reduced from 4.92 to 2.39 nm after the introduction of ATO. Afterward, the grain size of Pt increased to 6.78 nm with increasing Sb doping. The former may have been dominated by the strong interaction between Pt and ATO, and the latter may have been associated with the reduction in surface area and enhanced agglomeration of ATO at the amount of doped Sb increased.

The FE-SEM images in Fig. 2a and d depict the Pt/C-ATO 5% and 20% catalysts, respectively. These images provide visual evidence of the uniform distribution of Pt and ATO nanoparticles on the carbon black support.

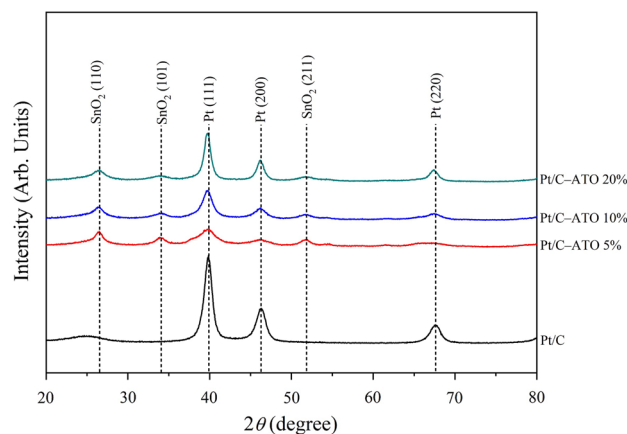


Figure 1. XRD patterns of Pt/C and Pt/C-ATO catalysts.

Catalyst	Pt grain size (nm)	ATO grain size (nm)
Pt/C	4.92	–
Pt/C-ATO 5%	2.39	4.77
Pt/C-ATO 10%	4.21	3.75
Pt/C-ATO 20%	6.78	3.45

Table 1. The grain size of Pt/C and various Pt/C-ATO catalysts.

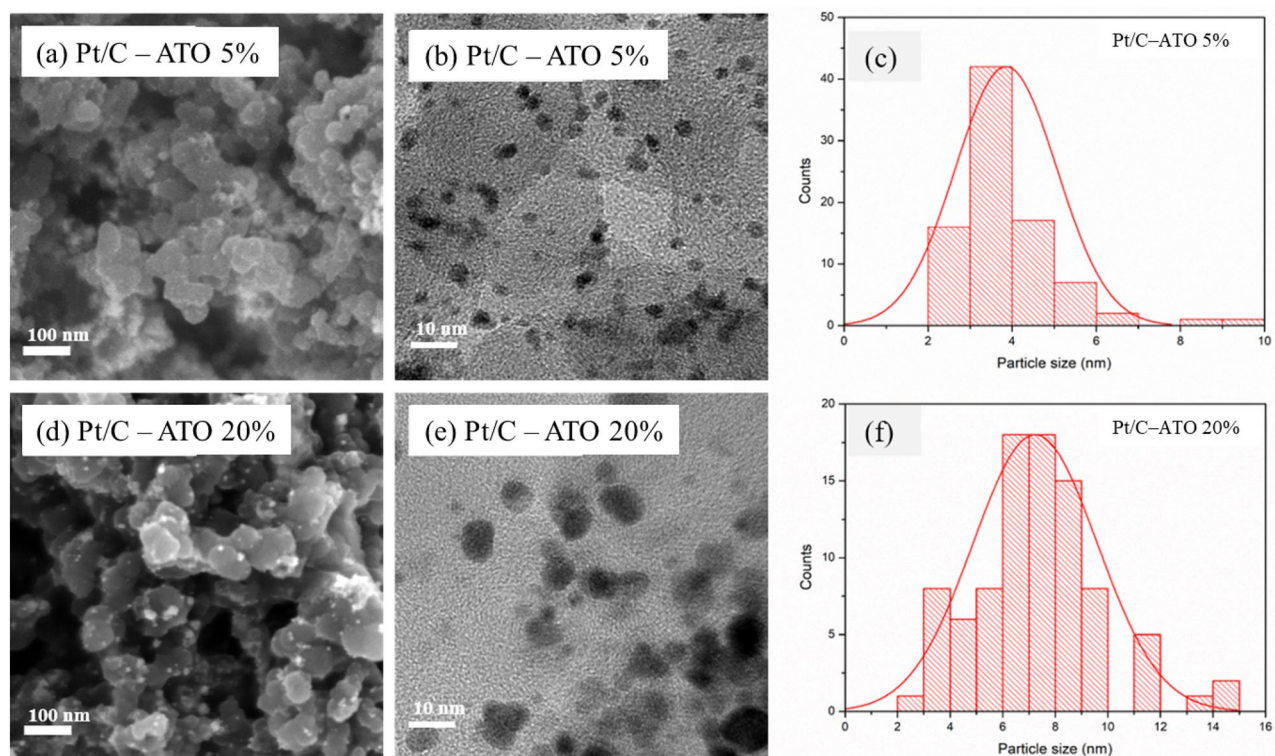


Figure 2. SEM, TEM images, and size distributions of (a–c) Pt/C–ATO 5% and (d–f) Pt/C–ATO 20% catalysts.

Notably, the Pt/C–ATO 20% exhibits visible particle agglomeration, signifying distinctive features associated with this specific composition. The TEM images and corresponding particle size distribution histograms of the Pt/C–ATO 5% and 20% samples are presented in Fig. 2b,c and Fig. 2e,f, respectively. The Pt and ATO nanoparticles in Pt/C–ATO 5% sample exhibited excellent dispersion on the supports, accompanied by a narrow particle size distribution. Additionally, a certain extent of stacking configuration was observed between the Pt and ATO nanoparticles. The average particle size of Pt was determined by directly measuring 100 isolated particles, which yielded an estimated value of approximately 3.86 nm. Although the majority of the Pt and ATO nanoparticles in Pt/C–ATO 20% maintained uniform dispersion on the carbon support, evidence of agglomeration was obtained from a subset of larger particles. The average particle size of Pt increased, reaching a value of 7.23 nm. At an optimal doping level, the dispersion of ATO particles on the surface of carbon black enhances surface heterogeneity and provides additional anchoring points, facilitating the formation of smaller Pt particles. However, when the concentration of ATO particles becomes excessive, their interparticle interactions may promote the formation of larger agglomerates, leading to the localized accumulation and clustering of Pt particles in these regions. The TEM observations are in agreement with the aforementioned SEM and XRD findings.

The high-resolution TEM image of the Pt/C–ATO 20% catalyst is presented in Fig. 3. Two distinct lattice fringes measuring 0.24 and 0.34 nm were observed, indicating the presence of crystal planes corresponding to Pt (111) and SnO₂ (110), respectively. The ATO supports effectively served as anchors for the Pt nanoparticles. Specifically, the Pt particles were primarily localized at the boundaries between ATO and carbon black. The emergence of this special triple-junction structure can have a crucial impact that can enhance the stability and activity of Pt catalysts for MORs³⁹.

To shed light on the underlying mechanism behind the promotional role of C–ATO composite supports, XPS was employed to analyze the electronic properties of the Pt catalysts investigated in this study. The high-resolution XPS analysis presented in Fig. 4 involved the deconvolution of the Pt 4f signals in various catalysts, revealing three distinct components assigned to Pt⁰, Pt²⁺, and Pt⁴⁺ representing metallic Pt, Pt(OH)₂, and PtO₂ like species, respectively²⁷. The binding energies of Pt 4f^{7/2}, in conjunction with the relative intensity ratio of Pt for each catalyst, are summarized in Table 2. The binding energy values of Pt 4f^{7/2}, in conjunction with the relative intensity ratio of Pt for each catalyst, are summarized in Table 2. The binding energy values of all peaks were meticulously aligned with the C 1 s peak position at 284.6 eV, serving as a reference point. The binding energy of metallic Pt in Pt/C–ATO is negatively shifted compared to Pt/C, providing strong evidence for the occurrence of electron transfer from ATO to Pt at Pt/C–ATO triple-junction nanostructures³⁷. This effect elevates the Fermi level or reduces Pt d-vacancy within a valence bond (5d orbital)^{40,41}.

Figure 5 schematically illustrates the mechanism of charge transfer between Pt and ATO. A Schottky junction is created when metallic Pt comes into contact with semiconductor ATO, resulting in a barrier that inhibits the flow of electrons. Owing to the higher Fermi level of Pt compared with ATO, a built-in electric field is created. In this study, the interface barrier and defects between Pt and ATO is not high, allowing the electric field to drive electron flow from ATO to Pt. The ATO sample with a higher level of Sb doping provides more electrons

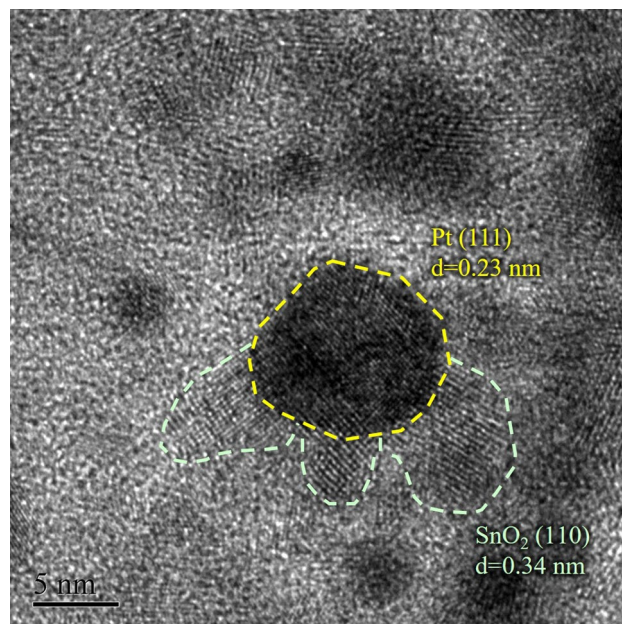


Figure 3. HR-TEM image of Pt/C-ATO 20% catalyst.

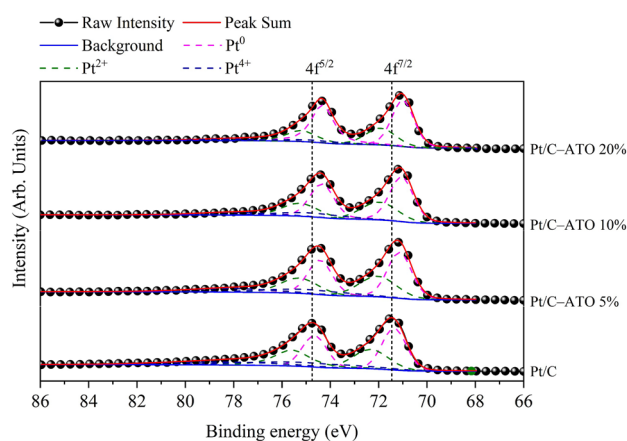


Figure 4. XPS Pt 4f spectra of Pt/C and Pt/C-ATO catalysts.

Catalyst	Pt ⁰		Pt ²⁺		Pt ⁴⁺	
	BE (eV)	Ratio (%)	BE (eV)	Ratio (%)	BE (eV)	Ratio (%)
Pt/C	71.36	43.61	72.33	35.54	75.16	20.85
Pt/C-ATO 5%	71.14	49.28	72.03	33.61	74.90	17.11
Pt/C-ATO 10%	71.05	56.02	71.97	31.22	74.79	12.76
Pt/C-ATO 20%	70.10	64.84	71.92	28.34	74.74	6.82

Table 2. The binding energy (eV) and related composition ratio (%) from deconvolution of XPS spectra for Pt 4f region of Pt/C and various Pt/C-ATO catalysts.

available for transfer, thereby enhancing the charge transfer in the Pt-ATO junction. The modification of the charge density and electronic properties at the Pt surface in a Schottky junction has several beneficial effects. First, they reduce the adsorption of poisoning species, such as CO, on the surface of a Pt catalyst and thus help maintain the availability of active sites for desired reactions^{42–44}. Second, the incorporated ATO enhances the occupancy of the Pt d-band, thereby weakening the Pt-O bond strength. Consequently, the weakened Pt-O

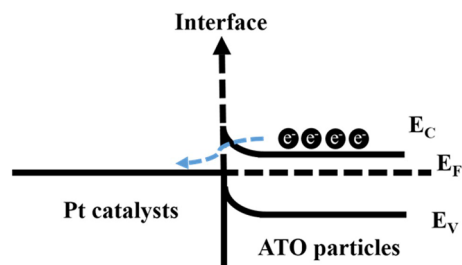


Figure 5. Schematic energy level diagrams for a Pt–ATO interface.

bond promotes the cleavage of O–O bonds, facilitating the reaction with OH^- to form H_2O at elevated potential and releasing Pt active sites^{45,46}. Third, the weakening of Pt–O bond strength provides a favorable condition that promote increase in metallic Pt content. As the level of Sb doping increased, the ratio of metallic Pt showed a gradual increase from 43.6% in Pt/C to 64.8% in Pt/C–ATO 20%, as shown in Table 2. This finding serves as additional evidence for the robust metal–support interactions between Pt and ATO^{37,47}. Finally, when ATO is incorporated into a system, it introduces additional oxygen vacancies and promotes the formation of hydroxyl groups (OH^-) on its surface. By enriching the presence of hydroxyl groups through ATO incorporation, the availability of surface oxygen species is enhanced, facilitating the reaction between poisoning CO intermediates adsorbed on Pt sites and these oxygen species; this effect is typically attributed to the bifunctional mechanism⁴⁸, the “ligand effect”⁴⁹, or a synergistic combination of these factors²⁸. The co-catalysis effect provided by the above-mentioned metal–semiconductor junction can enhance the overall catalytic activity of a Pt catalyst, facilitating efficient fuel utilization and improving the stability of fuel-cell systems.

The doping level of Sb in ATO was determined using XPS, revealing Sb doping amounts of 3.4%, 7.3%, and 13.5% for ATO-5%, ATO-10%, and ATO-20% particles, respectively. ATO-5%, ATO-10%, and ATO-20% particles exhibited electrical conductivity of 0.07, 0.21, and 0.13 S/cm, respectively, which were lower than the electrical conductivity of carbon black. When Sb is doped into SnO_2 , it takes on a donor role by substituting Sn and carrying a positive charge, resulting in Sb^{5+} . Given the unique electronic structure of Sb^{5+} , it donates additional electrons to the conduction band of a SnO_2 structure. These extra electrons move within the conduction band, enhancing its electrical conductivity. As the level of Sb doping increases, the Sb^{5+} dopant gradually gives way to Sb^{3+} , which acts as a compensating species for oxygen vacancies and consequently lowers electrical conductivity⁵⁰. Moreover, the presence of excessive lattice defects, internal stress, and amorphous antimony oxide can contribute to decline in the electrical conductivity of ATO.

Figure 6a shows the cyclic voltammograms of the Pt/C and Pt/C–ATO catalysts in a 0.5 M H_2SO_4 solution. The potential range from -0.4 to 1.2 V exhibited distinct and well-defined hydrogen adsorption/desorption peaks. In a polycrystalline Pt electrode, multiple hydrogen absorption peaks are usually observed due to the presence of various crystal facets. However, if the electrode surface is predominantly composed of a specific crystal facet or exhibits a poorer crystallinity, there may be only one main hydrogen absorption peak^{38,51}. The calculation of the ECSA of the Pt catalyst per unit weight of Pt was performed using the following equation.

$$\text{ECSA} = \frac{Q_{\text{H}} (\mu\text{C}/\text{cm}^2)}{210 (\mu\text{C}/\text{cm}^2) \times W_{\text{Pt}} (\text{mg}/\text{cm}^2)}$$

where Q_{H} is the charge of the absorption or desorption hydrogen on Pt surface, which corresponds to the area of cathode peak during the negative scan or anode peaks during the positive scan; W_{Pt} is the Pt loading by mass weight on the effective reaction area of the working electrode. ECSA is determined by extrapolation of the double-layer charging current from the region between 0.2 and 0.4 V back to about -0.2 V and integrating the charge for oxidation of adsorbed hydrogen on a positive-going potential sweep. The ECSA values of Pt/C, Pt/C–ATO 5%, Pt/C–ATO 10%, and Pt/C–ATO 20% were 55.97, 55.45, 68.14, and 35.57 m^2/g , respectively. The addition of ATO can improve the catalytic activity of Pt/C catalysts, increasing their efficiency in oxidation–reduction reactions. However, if the level of Sb doping is insufficient, ATO may exhibit poor conductivity, which decreases efficiency in oxidation–reduction reactions. When Sb doping exceeds the optimal level, it promotes the growth of the grain size of Pt, along with agglomeration and poor dispersion on the carbon support, resulting in a decrease in the utilization of Pt. In combination with the deteriorated electrical conductivity caused by excessive doping, a significant decrease in ECSA was observed. The Pt/C–ATO 10% catalyst achieved an optimal ECSA of 68.14 m^2/g as a result of the well-balanced conductivity, active surface area, and metal–support interaction. Stability is a significant challenge in PEMFC technology. To assess the electrochemical stability of the prepared samples, CV with up to 1000 cycles was determined. Figure 6b illustrates loss in the relative ECSA of the Pt/C, Pt/C–ATO 5%, Pt/C–ATO 10%, and Pt/C–ATO 20% catalysts after 200, 500, and 1000 cycles. As the cycling progressed, a pronounced decrease in ECSA was observed for Pt/C, whereas Pt/C–ATO showed a gradual decline. In Pt/C, the total ECSA loss was approximately 42%, whereas in Pt/C–ATO, the loss was reduced to 28%. The findings suggested that using a combination of carbon black and ATO as a support provides results in electrochemical stability approximately 1.23 times that obtained when carbon black alone is used. This enhanced durability can be attributed to the superior corrosion resistance of ATO in an acidic environment, as well as the strong interaction between Pt and ATO.

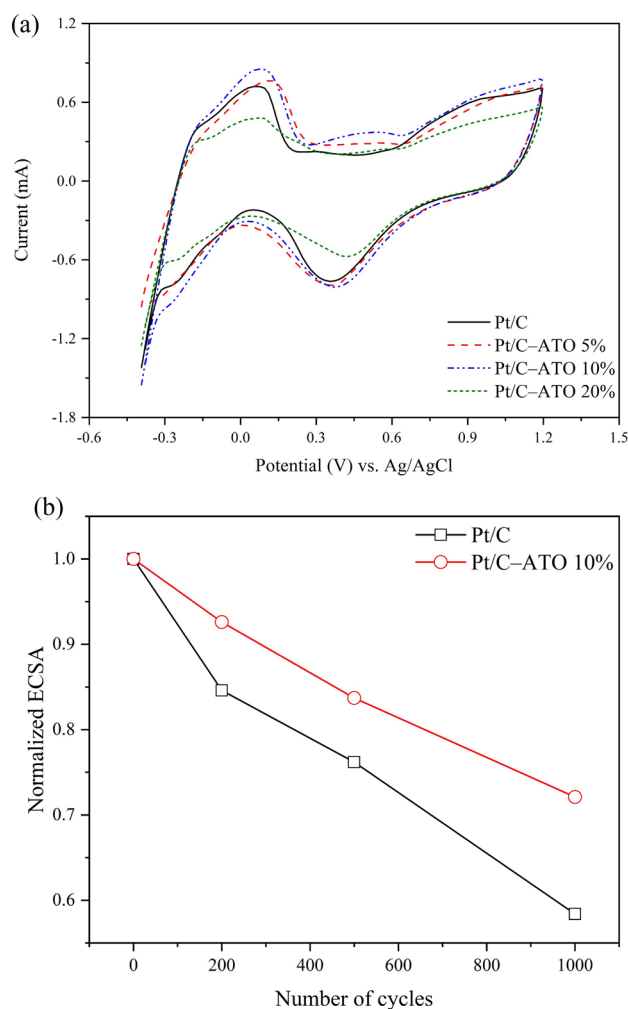


Figure 6. (a) Cyclic voltammogram of Pt/C and Pt/C-ATO catalysts in a 0.5 M H_2SO_4 solution. (b) Normalized ECSA of Pt/C and Pt/C-ATO 10% catalysts as a function of cycles.

To evaluate catalyst activity in methanol electrooxidation, steady-state polarization plots were obtained for Pt/C and Pt/C-ATO 10% catalysts in a solution containing 0.5 M H_2SO_4 and 1.0 M CH_3OH , as shown in Fig. 7. The Pt/C-ATO 10% catalyst exhibits an onset oxidation potential of 0.413 V for MOR, and Pt/C catalyst has an onset oxidation potential of 0.478 V. This result suggested that MOR preferentially occurred on the Pt/C-ATO 10% catalyst. The peak current for MOR on the Pt/C-ATO 10% catalyst was 4.63 mA, which is 1.29 times the peak current observed on the Pt/C catalyst (3.59 mA), indicating the enhancing effect of ATO on the electrooxidation of methanol. The CO tolerance of Pt catalyst can be assessed by analyzing the current peak ratio of I_f (forward peak current density) to I_b (backward current peak density), represented as I_f/I_b ⁵². Pt/C-ATO 10% exhibited a higher I_f/I_b ratio of 1.30 compared to the I_f/I_b ratio of 1.03 for Pt/C, indicating better efficiency in methanol oxidation to carbon dioxide and reduced accumulation of carbonaceous residues on the Pt surface. The results of onset oxidation potential, peak current, and I_f/I_b ratio values demonstrated that the Pt/C-ATO 10% catalyst exhibited superior electrocatalytic activity and CO tolerance for MOR.

The cell performance of Pt/C and Pt/C-ATO catalysts was examined under room temperature, which closely mimicked a nonhumidified state ($\text{RH} = 0\%$), as shown in Fig. 8. The results directly verified the self-humidification capability of the MEA^{53,54}. The current densities obtained at 0.6 V exhibited the following trend: Pt/C-ATO 10% > Pt/C > Pt/C-ATO 5% > Pt/C-ATO 20%. The Pt/C-ATO 10% catalyst exhibited a maximum power density of 0.39 W cm^{-2} , surpassing the Pt/C catalyst (0.34 W cm^{-2}) by 15%. These findings are consistent with the cyclic voltammograms measurements. Electrical conductivity, active surface area, and intrinsic activities are crucial factors that influence the cell performance of catalysts. Although the Pt/C-ATO 5% demonstrates a finer granularity of Pt particles, this advantage is offset by a lower electrical conductivity, resulting in virtually no change in electrochemical activity^{51,55}. Despite the lower electrical conductivity and surface area of ATO compared with carbon black, the Pt/C-ATO 10% samples demonstrated higher surface specific activities. This result suggested that the higher intrinsic activities of Pt/C-ATO 10% outweighed the negative effect of the lower electrical conductivity and surface area of ATO, making the catalyst a promising catalyst support material in PEMFCs.

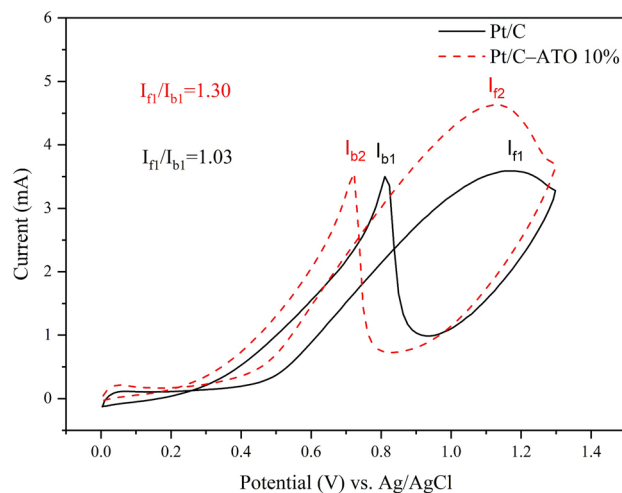


Figure 7. Cyclic voltammogram of Pt/C and Pt/C-ATO 10% catalysts in a 0.5 M H₂SO₄ + 1.0 M CH₃OH solution.

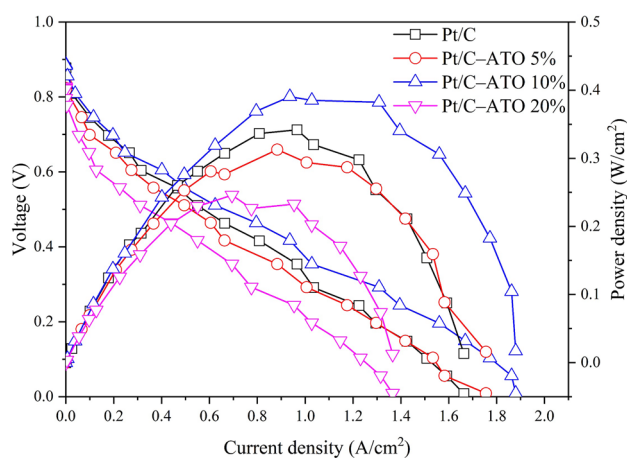


Figure 8. Polarization and power density curves of Pt/C and Pt/C-ATO catalysts.

Conclusion

In this work, Pt and ATO nanoparticles were simultaneously precipitated onto the surface of carbon black for the fabrication of a highly effective catalyst for PEMFCs. The influences of Sb doping on the crystal, structural, electrochemical characteristics of the ATO particles were examined. Through the proper incorporation of Sb dopants, ATO exhibited a remarkable increase in electrical conductivity while maintaining uniform dispersion on the carbon support without evident agglomeration or coalescence. The C-ATO-supported Pt nanoparticles exhibited a negative shift in the binding energy of Pt 4f and a higher ratio of metallic Pt owing to the formation of unique Pt/C-ATO triple-junction nanostructures and strong interaction with ATO. Accordingly, the Pt/C-ATO catalysts exhibited significantly enhanced electrochemical activity, durability, and CO tolerance compared with the Pt/C catalyst according to the CV measurements. The MEA samples containing a composite support of carbon and ATO in the catalyst layer exhibited a power density up to 15% higher than that of the MEA lacking ATO particles, indicating that achieving optimal cell performance relies on finding the right balance among electrical conductivity, active surface area, and intrinsic activity.

Data availability

The datasets generated during and/or analysed during the current study are available from the corresponding author on reasonable request.

Received: 28 August 2023; Accepted: 15 December 2023

Published online: 27 December 2023

References

- Jacobson, M. Z., Colella, W. G. & Golden, D. M. cleaning the air and improving health with hydrogen fuel-cell vehicles. *Science* **308**, 1901–1905 (2005).
- Murphy, O. J., Hitchens, G. D. & Manko, D. J. High power density proton-exchange membrane fuel cells. *J. Power Sources* **47**, 353–368 (1994).
- Peighambari, S. J., Rowshanzamir, S. & Amjadi, M. Review of the proton exchange membranes for fuel cell applications. *Int. J. Hydrog. Energy* **35**, 9349–9384 (2010).
- Wilberforce, T. *et al.* Developments of electric cars and fuel cell hydrogen electric cars. *Int. J. Hydrog. Energy* **42**, 25695–25734 (2017).
- Rosso, I., Galletti, C., Saracco, G., Garrone, E. & Specchia, V. Development of A zeolites-supported noble-metal catalysts for CO preferential oxidation: H₂ gas purification for fuel cell. *Appl. Catal. B Environ.* **48**, 195–203 (2004).
- Cheah, S. K., Bernardet, V. P., Franco, A. A., Lemaire, O. & Gelin, P. Study of CO and hydrogen interactions on carbon-supported Pt nanoparticles by quadrupole mass spectrometry and operando diffuse reflectance FTIR spectroscopy. *J. Phys. Chem. C* **117**, 22756–22767 (2013).
- Tilquin, J. Y., Côté, R., Guay, D., Dodelet, J. P. & Denès, G. Carbon monoxide poisoning of platinum-graphite catalysts for polymer electrolyte fuel cells: Comparison between platinum-supported on graphite and intercalated in graphite. *J. Power Sources* **61**, 193–200 (1996).
- Shi, W., Yi, B., Hou, M. & Shao, Z. The effect of H₂S and CO mixtures on PEMFC performance. *Int. J. Hydrog. Energy* **32**, 4412–4417 (2007).
- Oetjen, H. F., Schmidt, V. M., Stimming, U. & Trila, F. Performance data of a proton exchange membrane fuel cell using H₂/CO as fuel gas. *J. Electrochem. Soc.* **143**, 3838 (1996).
- Pantea, D., Darmstadt, H., Kaliaguine, S., Sümmerchen, L. & Roy, C. Electrical conductivity of thermal carbon blacks: Influence of surface chemistry. *Carbon* **39**, 1147–1158 (2001).
- Kinoshita, K. in *Carbon: Electrochemical and Physicochemical Properties*, (New York, 1988).
- Oh, H. S., Lee, J. H. & Kim, H. Electrochemical carbon corrosion in high temperature proton exchange membrane fuel cells. *Int. J. Hydrog. Energy* **37**, 10844–10849 (2012).
- Borup, R. L., Davey, J. R., Garzon, F. H., Wood, D. L. & Inbody, M. A. PEM fuel cell electrocatalyst durability measurements. *J. Power Sources* **163**, 76–81 (2006).
- Wang, J. *et al.* Effect of carbon black support corrosion on the durability of Pt/C catalyst. *J. Power Sources* **171**, 331–339 (2007).
- Zhang, Z., Liu, J., Junjie, Gu., Liang, Su. & Cheng, L. An overview of metal oxide materials as electrocatalysts and supports for polymer electrolyte fuel cells. *Energy Environ. Sci.* **7**, 2535–2558 (2014).
- Antolini, E. & Gonzalez, E. R. Ceramic materials as supports for low-temperature fuel cell catalysts. *Solid State Ionics* **180**, 746–763 (2009).
- Zhao, X. *et al.* Recent advances in catalysts for direct methanol fuel cells. *Energy Environ. Sci.* **4**, 2736–2753 (2011).
- Yin, S., Shichun, Mu., Lv, H., Niancai Cheng, Mu. & Pan, Z. F. A highly stable catalyst for PEM fuel cell based on durable titanium diboride support and polymer stabilization. *Appl. Catal. B Environ.* **93**, 233–240 (2010).
- Hepel, M., Dela, I., Hepel, T., Luo, J. & Zhong, C. J. Novel dynamic effects in electrocatalysis of methanol oxidation on supported nanoporous TiO₂ bimetallic nanocatalysts. *Electrochim. Acta* **52**, 5529–5547 (2007).
- Ignaszak, A. *et al.* Carbon–Nb_{0.07}Ti_{0.93}O₂ composite supported Pt–Pd electrocatalysts for PEM fuel cell oxygen reduction reaction. *Electrochim. Acta* **75**, 220–228 (2012).
- Dou, M. *et al.* SnO₂ nanocluster supported Pt catalyst with high stability for proton exchange membrane fuel cells. *Electrochim. Acta* **92**, 468–473 (2013).
- Motou, S., Shibata, M. & Watanabe, M. Electrocatalysis by ad-atoms: Part VI. Enhancement of CO oxidation on Pt(subs) and Pt–Au(subs) electrodes by Sn ad-atoms. *J. Electroanal. Chem. Interfacial Electrochem.* **110**, 103–109 (1980).
- Matsui, T. *et al.* Electrochemical oxidation of CO over tin oxide supported platinum catalysts. *J. Power Sources* **155**, 152–156 (2006).
- Okanishi, T., Matsui, T., Takeguchi, T., Kikuchi, R. & Eguchi, K. Chemical interaction between Pt and SnO₂ and influence on adsorptive properties of carbon monoxide. *Appl. Catal. A Gen.* **298**, 181–187 (2006).
- Jiang, Z.-Z., Wang, Z.-B., Chu, Y.-Y., Da-Ming, Gu. & Yin, G.-P. Ultrahigh stable carbon riveted Pt/TiO₂–C catalyst prepared by in situ carbonized glucose for proton exchange membrane fuel cell. *Energy Environ. Sci.* **4**, 728–735 (2011).
- Shanmugam, S. & Gedanken, A. Carbon-coated anatase TiO₂ nanocomposite as a high-performance electrocatalyst support. *Small* **3**, 1189–1193 (2007).
- Qin, Y.-H. *et al.* Enhanced methanol oxidation activity and stability of Pt particles anchored on carbon-doped TiO₂ nanocoating support. *J. Power Sources* **278**, 639–644 (2015).
- Li, Y. *et al.* Sn-doped TiO₂ modified carbon to support Pt anode catalysts for direct methanol fuel cells. *J. Power Sources* **286**, 354–361 (2015).
- Wang, Y. *et al.* Superior catalytic performance and CO tolerance of Ru@Pt/C–TiO₂ electrocatalyst toward methanol oxidation reaction. *Appl. Surface Sci.* **473**, 943–950 (2019).
- Sandoval-González, A., Borja-Arco, E., Jaime Escalante, O. & Jiménez-Sandoval, S. A. G. Methanol oxidation reaction on PtSnO₂ obtained by microwave-assisted chemical reduction. *Int. J. Hydrog. Energy* **37**, 1752–1759 (2012).
- Lee, K.-S. *et al.* Electrocatalytic activity and stability of Pt supported on Sb-doped SnO₂ nanoparticles for direct alcohol fuel cells. *J. Catal.* **258**, 143–152 (2008).
- Scherrer, P. Bestimmung der inneren Struktur und der Größe von Kolloidteilchen mittels Röntgenstrahlen. In *Kolloidchemie Ein Lehrbuch* (ed. Zsigmondy, R.) 387–409 (Springer, 1912).
- Wang, Y., Brezesinski, T., Antonietti, M. & Smarsly, B. Ordered mesoporous Sb-, Nb-, and Ta-Doped SnO₂ thin films with adjustable doping levels and high electrical conductivity. *ACS Nano* **3**, 1373–1378 (2009).
- Saha, M. S., Li, R., Cai, M. & Sun, X. high electrocatalytic activity of platinum nanoparticles on SnO₂ nanowire-based electrodes. *Electrochem. Solid-State Lett.* **10**, B130 (2007).
- Daio, T. *et al.* Lattice strain mapping of platinum nanoparticles on Carbon and SnO₂ supports. *Sci. Reports* **5**, 13126 (2015).
- Novomlinskiy, I. N., Danilenko, M. V., Safronenko, O. I., Tabachkova, NYu. & Guterman, V. E. Influence of the Sn-Oxide-carbon carrier composition on the functional characteristics of deposited platinum electrocatalysts. *Electrocatalysis* **12**, 489–498 (2021).
- Yin, M. *et al.* Highly active and stable Pt electrocatalysts promoted by antimony-doped SnO₂ supports for oxygen reduction reactions. *Appl. Catal. B Environ.* **144**, 112–120 (2014).
- Dhanasekaran, P., Vinod Selvaganesh, S., Sarathi, L. & Bhat, S. D. Rutile TiO₂ supported Pt as stable electrocatalyst for improved oxygen reduction reaction and durability in polymer electrolyte fuel cells. *Electrocatalysis* **7**, 495–506 (2016).
- Kou, R. *et al.* Stabilization of electrocatalytic metal nanoparticles at metal–metal oxide–graphene triple junction points. *J. Am. Chem. Soc.* **133**, 2541–2547 (2011).
- Caixia, Xu., Wang, L., Xiaolei, Mu. & Ding, Yi. Nanoporous PtRu alloys for electrocatalysis. *Langmuir* **26**, 7437–7443 (2010).
- Igarashi, H., Fujino, T., Zhu, Y., Uchida, H. & Watanabe, M. CO Tolerance of Pt alloy electrocatalysts for polymer electrolyte fuel cells and the detoxification mechanism. *Phys. Chem. Chem. Phys.* **3**, 306–314 (2001).

42. Navarro, R. M., Álvarez-Galván, M. C., Cruz Sánchez-Sánchez, M., Rosa, F. & Fierro, J. L. G. Production of hydrogen by oxidative reforming of ethanol over Pt catalysts supported on Al₂O₃ modified with Ce and La. *Appl. Catal. B Environ.* **55**, 229–241 (2005).
43. Haan, J. L., Stafford, K. M. & Masel, R. I. Effects of the addition of antimony, Tin, and Lead to Palladium catalyst formulations for the direct formic acid fuel cell. *J. Phys. Chem. C* **114**, 11665–11672 (2010).
44. Zhang, Z. *et al.* Highly active Carbon-supported PdSn catalysts for formic acid electrooxidation. *Fuel Cells* **9**, 114–120 (2009).
45. Zhang, Na. *et al.* Pt/Tin Oxide/Carbon nanocomposites as promising oxygen reduction electrocatalyst with improved stability and activity. *Electrochim. Acta* **117**, 413–419 (2014).
46. Hammer, B. & Nørskov, J.K. Theoretical surface science and catalysis—Calculations and concepts. In *Advances in Catalysis*, 71–129 (Academic Press, 2000).
47. Lv, Q. *et al.* Promotion effect of TiO₂ on catalytic activity and stability of Pt catalyst for electrooxidation of methanol. *J. Power Sources* **218**, 93–99 (2012).
48. Watanabe, M. & Motoo, S. Electrocatalysis by ad-atoms: Part II Enhancement of the oxidation of methanol on platinum by ruthenium ad-atoms. *J. Electroanal. Chem. Interfacial Electrochem.* **60**, 267–273 (1975).
49. Frelink, T., Visscher, W. & van Veen, J. A. R. On the role of Ru and Sn as promoters of methanol electro-oxidation over Pt. *Surface Sci.* **335**, 353–360 (1995).
50. Terrier, C., Chatelon, J. P., Berjoan, R. & Roger, J. A. Sb-doped SnO₂ transparent conducting oxide from the sol-gel dip-coating technique. *Thin Solid Films* **263**, 37–41 (1995).
51. Shahgaldi, S. & Hamelin, J. The effect of low platinum loading on the efficiency of PEMFC's electrocatalysts supported on TiO₂-Nb, and SnO₂-Nb: An experimental comparison between active and stable conditions. *Energy Convers. Manag.* **103**, 681–690 (2015).
52. Liu, Z., Ling, X. Y., Su, X. & Lee, J. Y. Carbon-supported Pt and PtRu nanoparticles as catalysts for a direct methanol fuel cell. *J. Phys. Chem. B* **108**, 8234–8240 (2004).
53. Chao, W.-K. *et al.* Improvement of the proton exchange membrane fuel cell (PEMFC) performance at low-humidity conditions by adding hygroscopic γ -Al₂O₃ particles into the catalyst layer. *J. Power Sources* **185**, 136–142 (2008).
54. Huang, R.-H. *et al.* Improvement of proton exchange membrane fuel cells performance by coating hygroscopic zinc oxide on the anodic catalyst layer. *J. Power Sources* **227**, 229–236 (2013).
55. Akalework, N. G. *et al.* Ultrathin TiO₂-coated MWCNTs with excellent conductivity and SMSI nature as Pt catalyst support for oxygen reduction reaction in PEMFCs. *J. Mater. Chem.* **22**, 20977–20985 (2012).

Acknowledgements

The authors are thankful to National Science and Technology Council of Taiwan for funding this work through the Researchers Supporting Project, project number 111-2221-E-005-049-MY3. The authors are also thankful to Core Facility Center of National Cheng Kung University of Taiwan for partial support.

Author contributions

Data curation; Formal analysis; Investigation; Visualization; Writing—original draft: D.C.T. Writing—original draft; Project administration; Supervision: B.H.K. Formal analysis; Investigation; Visualization: H.P.C. Conceptualization; Resources; Validation: E.C.C. Funding acquisition; Project administration; Resources; Supervision; Writing—review & editing: F.S.S.

Competing interests

The authors declare no competing interests.

Additional information

Correspondence and requests for materials should be addressed to F.-S.S.

Reprints and permissions information is available at www.nature.com/reprints.

Publisher's note Springer Nature remains neutral with regard to jurisdictional claims in published maps and institutional affiliations.



Open Access This article is licensed under a Creative Commons Attribution 4.0 International License, which permits use, sharing, adaptation, distribution and reproduction in any medium or format, as long as you give appropriate credit to the original author(s) and the source, provide a link to the Creative Commons licence, and indicate if changes were made. The images or other third party material in this article are included in the article's Creative Commons licence, unless indicated otherwise in a credit line to the material. If material is not included in the article's Creative Commons licence and your intended use is not permitted by statutory regulation or exceeds the permitted use, you will need to obtain permission directly from the copyright holder. To view a copy of this licence, visit <http://creativecommons.org/licenses/by/4.0/>.

© The Author(s) 2023